International Forum on Aeroelasticity and Structural Dynamics
10-13 June 2019, Savannah, Georgia - USA

INVESTIGATION OF GUST LOADS ON A FLEXIBLE FORWARD SWEPT WING

Vega Handojo[1], Yasser M. Meddaikar[2], Johannes K.S. Dillinger[3], Jurij Sodja[4], Roeland De Breuker[5]

[1] DLR – Institute of Aeroelasticity, Göttingen, Germany, vega.handojo@dlr.de
[2] DLR – Institute of Aeroelasticity, Göttingen, Germany, muhammad.meddaikar@dlr.de
[3] DLR – Institute of Aeroelasticity, Göttingen, Germany, johannes.dillinger@dlr.de
[4] Delft University of Technology – Faculty of Aerospace Engineering, j.sodja@tudelft.nl
[5] Delft University of Technology – Faculty of Aerospace Engineering, r.debreuker@tudelft.nl

Keywords: Gust generator, dynamic gust loads, forward swept wing.

Abstract: This paper presents a semi-experimental method which can be used to predict the gust response of a wind tunnel model. The method incorporates transfer functions of the wind tunnel model – in this case a flexible forward swept wing – which are obtained using sweep excitations with a gust generator. The prediction results are then compared with those resulting from experimental measurements and numerical simulations. The observed quantities comprise accelerations and loads data. In the ideal case, the advantage of this semi-experimental prediction of the wing's response to gusts lies mainly in the reduction of wind tunnel time. Instead of testing each gust profile at each frequency, a measurement of several sweep excitations would suffice.

1 INTRODUCTION

Since 1994, dynamic gusts have been a part of the design load conditions for the certification of large aircraft [1][2]. Therefore, it is of great importance to improve methods to measure dynamic gust loads in wind tunnel tests to collect data which are used to optimize the aircraft design. However, wind tunnel tests are expensive, particularly if the flow has to be transonic to represent a typical cruise flight condition of transport aircraft. Therefore, a method which can potentially reduce wind tunnel testing time is of great relevance.

At the same time, aircraft manufacturers have been striving to reduce the operational cost of the aircraft, among others by minimizing the fuel consumption. For this aspect, the DLR project ALLEGRA was initiated in 2012 to investigate the potential of natural laminar flow (NLF) combined with aeroelastic tailoring [3]. The NLF aspect originates from the DLR project LamAiR which incorporates a forward swept wing [4]. Aeroelastic tailoring has been extensively studied over the last few decades and encompasses the use of beneficial tailorable properties of composites. Within ALLEGRA, aeroelastic tailoring is applied to minimize the mass penalty of a forward swept wing configuration while complying with aeroelastic constraints. In that project, two aeroelastically tailored forward swept wings were optimized, manufactured, and static tests were conducted at the subsonic SWG wind tunnel in Göttingen. One of the two wings – which is used as the reference in this investigation – is made of glass-fiber composite and was designed for maximizing deflection while constraining the wing tip twist. The design of the wings was performed using an in-house aeroelastic optimization framework and has been presented by Meddaikar, Dillinger et al. [5]-[10].

To investigate the dynamic gust response behavior of the glass-fiber wing, wind tunnel tests were carried out at the OJF (Open Jet Facility) at Delft University of Technology in February

2018. The dynamic excitations of the wing – comprising sweep, discrete and continuous gust excitations – were performed using the gust generator developed at Delft University of Technology and presented by Lancelot et al. [12]0.
The main focus of this paper is the proposed semi-experimental approach which has the potential to reduce future wind tunnel testing time. To do so, the wing's responses to the sweep excitation are extracted, and the wing's transfer functions are approximated. Using the transfer functions, the wing's responses to any gust within the linear regimecan be predicted. The results are then compared with those resulting from experimental measurements and numerical simulations. In the analyses, the observed quantities comprise accelerations and loads data.

2 DESIGN AND MANUFACTURING OF AEROELASTICALLY TAILORED WING

2.1 Model Design

The wing model used in this experimental study is a forward-swept wing with a leading edge sweep angle of -15°, a semi-span of 1.6 m, root and tip chord of 0.36 m and 0.12 m respectively, a full wing aspect ratio of 13.33 and a custom airfoil. In order to tap the stiffness-tailoring potential of composites, the entire wing is designed having five design fields each in the upper and lower skin. Each design field is defined as a region having constant stiffness properties, effectively constant laminate stacking sequence. Laminate blending rules are followed in order to ensure ply continuity while manufacturing and improve structural integrity between the regions with varying laminates. The geometry of the wing and the distribution of the design fields are shown in Figure 1.

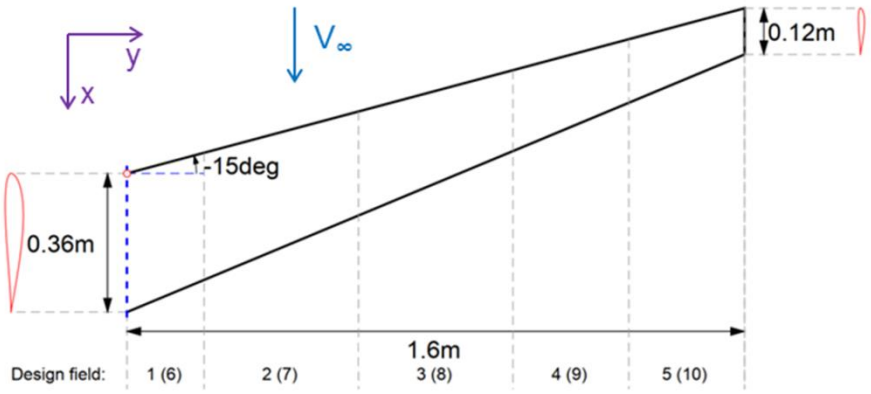

Figure 1: Wing planform showing distribution of the design fields in the skins (within brackets are the design field numbering in the lower skin)

The wing is tailored for maximum flexibility, while ensuring that the resulting twist-deformation at the tip is zero. The requirement on the twist is placed in the optimization, since forward-swept wings tend to produce a nose-up twist when bending upwards, which aggravates toward static aeroelastic instability in the form of wing divergence. Figure 2 shows the polar distribution of the A_{11} term in the ABD composite stiffness matrix of the upper skin. This distribution highlights the main direction of stiffness in the upper skin of the wing. In this case, it is a distribution characteristic of bend-twist coupling that aims to produce a nose-down twist when experiencing an upward-bending deflection. Details of the wing design and the DLR in-house aeroelastic tailoring framework are presented in [5]-[10].

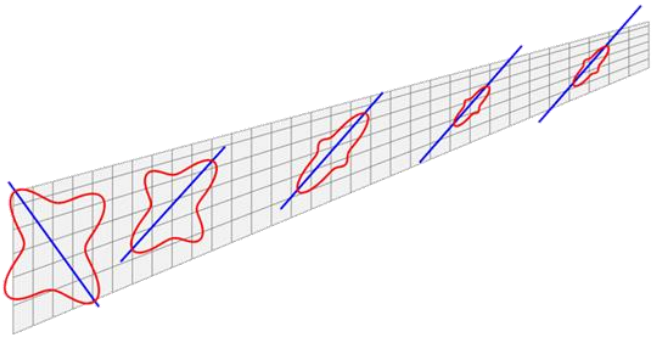

Figure 2: Distribution of stiffness term A_{11} in the upper skin

2.2 Manufacturing

With wing flexibility being the design objective of the wing, a uni-directional glass fiber material (E-glass/epoxy) is used in the design. A load-carrying skin concept is applied in order to keep the modelling and manufacturing simple, while a foam core (Styrodur 3035CS) filled between the upper and lower skin ensured structural stability. The wing is manufactured using a hand layup and vacuum-bagging technique.
An optic strain measurement fiber is placed along the 25%-chord line at the interface between the lower skin and the foam core. The strain fiber provides the capability of measuring strains with a very fine spatial distribution of close to 2 mm.

2.3 Previous tests

The forward-swept wing investigated in this study has been used extensively in previous tests.

- Static tests: span-wise deformation and strains were measured under different tip loading.
- GVT: eigen frequencies and mode-shapes were calculated using velocity data captured with a laser Doppler vibrometer (LDV). The results from these tests have been used to perform a structural model-update of the FE model [14].
- Wind-tunnel tests: static and dynamic test points were measured at different wind-velocities and angles of attack in the subsonic SWG tunnel in Göttingen [5]. The wind-tunnel tests showed a maximum displacement of close to 20% of the wing semi-span. The respective numerical investigations have been conducted by Ritter et al. [10].

2.4 Numerical model

Beside the wind tunnel model, its simulation model is also used in the numeric approach for a comparison with the experimental results. It consists of an MSC.Nastran finite element (FE) model of the aeroelastically tailored wing and its corresponding DLM (Doublet-Lattice-Method) aerodynamic model as shown in Figure 3. In this case, the FE-model is condensed onto its loads reference axis (LRA) nodes since the observed quantities such as wingtip acceleration and root loads only require the global stiffness and mass distribution on the wing. In Figure 3(a), the loads reference axis is marked by the thicker blue line. Moreover, the nodes at the leading and trailing edge are used to spline the aerodynamic forces onto the FE model. The leading and trailing edge nodes are rigidly connected with the corresponding LRA nodes, as indicated by the magenta lines.

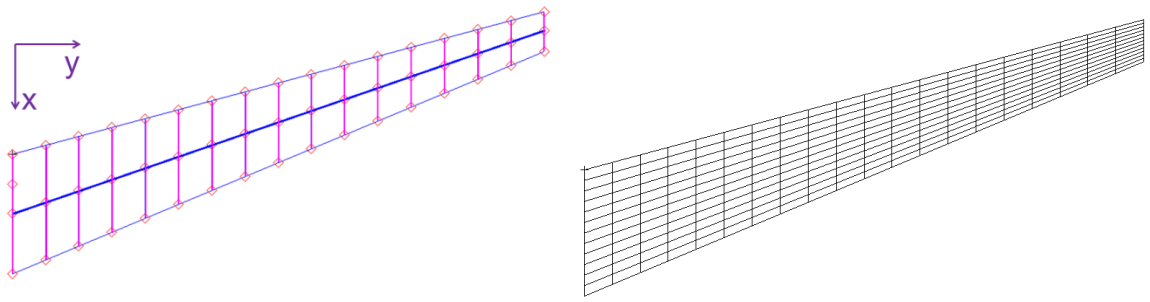

(a) (b)

Figure 3: Condensed FE model (a) and DLM model (b) of the wing

3 EXPERIMENTAL SETUP AND PREPARATIONS

3.1 Experimental setup

The experiment was performed in the Open Jet Facility (OJF) at Delft University of Technology. The wind tunnel features a test section of 2.85×2.85 m² and can achieve a maximum flow speed of 35 m/s. The experimental setup with the test wing mounted in the test chamber is shown in Figure 4. The design of the wing is presented in more detail in Section 2 while the rest of the test setup and the measurement procedure are presented below.

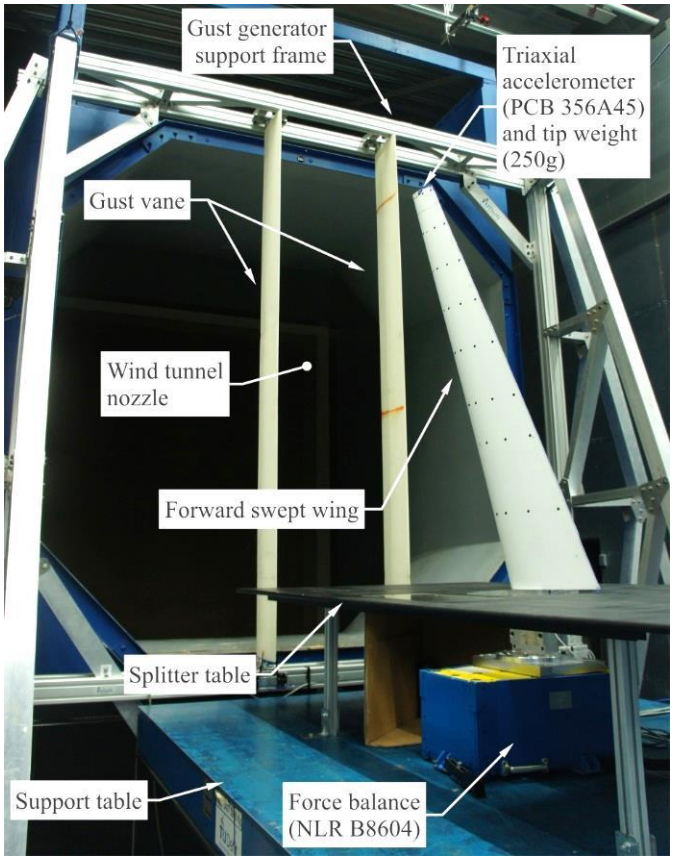

Figure 4: Experimental setup

The experimental setup consists of two main components: the gust generator and the response measurement system. The details about the characteristics of the gust generator were already presented in detail in [12]. The gust generator was used to provide aerodynamic excitation in the form of single-frequency continuous harmonic gust, discrete 1-cos gust and frequency-

sweep gust in the frequency range from 1 up to 9 Hz. The frequency range was selected such to encompass quasi-steady, unsteady and highly unsteady aerodynamic effects while still complying with the deflection rate and hinge moment constraints of the gust generator.
Dynamic response of the tested wing was investigated by measuring the unsteady loads at the root of the wing and the acceleration of the wing tip. Unsteady loads were measured using a six-component balance (NLR B8604) which properties are summarized in Table 1. The balance axis definitions and sign conventions are defined in Figure 5. It is noteworthy that the balance reference point BC is located 168.5 mm below the mount plate of the wing which must be accounted for in the calculation of the wing root moments.
Moreover, a splitter plate was installed at the root of the test wing in order to provide a clean airflow to the test wing and to shield the wing clamp and the balance from the airflow.

Table 1: Load balance properties

Component	Range†	Accuracy‡
F_x	$\pm$250 N	0.06%
F_y	$\pm$500 N	0.16%
F_z	$\pm$500 N	0.23%
M_x	±500 Nm	0.05%
M_y	$\pm$50 Nm	0.25%
M_z	$\pm$250 Nm	0.05%

†All components loaded simultaneously
‡Relative to the full-scale range

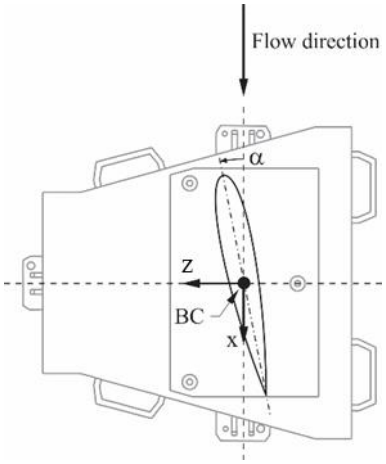

Figure 5: Balance axis system and sign convention

In addition to the load measurements, the wing acceleration was also measured using a triaxial accelerometer (PCB 356A45) mounted in the tip of the wing. The current accelerometer was selected due to its low mass, 4.2 grams, high sensitivity, 100 mV/g, and its broad frequency range, from 0.7 up to 10 kHz [15].

3.2 Model adaptation

The first wing bending mode of the FE model occurs at 12.6 Hz. With the gust generator exciting frequencies up to 9 Hz, no resonance would be evoked. Hence, the frequency of the first wing bending had to be decreased so that a resonance can emerge. To do so, a mass weighing 250 grams was added to the wingtip. With the additional mass, the first wing bending frequency decreases to 5.7 Hz which lies within the excitation range.
However, with oncoming flow in the wind tunnel, the resonance frequency of the first bending mode is expected to be slightly lower than 5.7 Hz due to aerodynamic effects. First simulations showed that – depending on the flow velocity which goes up to 30 m/s – a resonance would emerge between 5.4 Hz and 5.7 Hz. As a compromise, the excitation frequency of the gust generator which is intended to evoke resonance was set to 5.6 Hz.

3.3 Measurement procedure

Before dynamic gust excitations were introduced, static measurements of the wing in the wind tunnel were conducted. For this purpose, the incidence angle – which equals the angle of attack – of the clamped wing was varied, and the parameters are listed in Table 2.
To facilitate the semi-numerical and the experimental approach to predicting gust response of the test wing, three different excitations were used: continuous frequency-sweep gust with exponential frequency progression, single-frequency continuous harmonic gusts and discrete 1-cos gust. Gust parameters for each excitation method are summarized in Table 3.
The measurements were executed as follows. First, the wing was excited with the continuous frequency-sweep gust to determine the experimental transfer function between the gust and the wing tip acceleration and between the gust and the root loads. The so-obtained transfer functions were then used in the semi-numerical approach to synthesize the gust response of the wing to single-frequency continuous harmonic gust and the discrete 1-cos gust as explained in Section 5.
In the following step the wing was excited with a single-frequency continuous harmonic gust and a discrete 1-cos gust to measure the actual gust response of the wing in terms of root loads and wing tip acceleration. The measured responses then served for validation of the numerical and semi-experimental results as shown in Section 5.
The measurements were conducted at various static incidence angles and flow conditions as summarized in Table 3. The measurements were repeated for every combination of the listed incidence angles, flow velocities and gust parameters which amounts to 156 dynamic measurements in total.

Table 2: Static measurement parameters

Parameter	Value
Flow velocity in m/s	15, 23, 29
Incidence angle in deg	-10, -8,…, 14

Table 3: Dynamic measurement parameters

Parameter	Value
Flow velocity in m/s	15, 29
Incidence angle in deg	0, 4, 10
continuous frequency-sweep gust	
frequency range in Hz	1-9
gust vane amplitude in deg	±5; ±10
single-frequency continuous harmonic gusts	
frequency in Hz	1, 3, 5.6, 7
gust vane amplitude in deg	5, 10, 15
discrete 1-cos gust	
frequency in Hz	1, 3, 5.6, 7
gust vane amplitude in deg	5, 10, 15

4 METHODOLOGY

In this section, the focus lies on the derivation of the semi-experimental method which exploits the advantages of experiments – the collected data represents the actual wind tunnel model instead of the simulation model. At the same time, it helps in potentially reducing the wind tunnel time by using numerical tools to predict the wing's response. The approach mainly comprises the derivation of the transfer functions (TF) and their smoothing using a rational function approximation (RFA). Furthermore, subsequent mathematical operations to obtain the respective time responses are presented.

4.1 Transfer function derivation

To be able to derive the transfer functions (TF), the identification of the wing's dynamic response to gusts with a broad spectrum is necessary. To do so, geometric sweep excitations using the gust generator are introduced. Geometric or exponential sweep implies that the frequency ratio over a certain period of time is constant. As an example: if an increase from 1 to 2 Hz occurs within 10 seconds, an increase from 4 to 8 Hz also takes the same amount of time. Compared to a linear sweep, the geometric sweep bears the advantage that each frequency range has the same number of wave periods. As an example: in a linear sweep starting at 1 Hz which increases to 2 Hz in one period, it would take 10 periods to increase from 10 to 20 Hz. In this linear sweep case, a resonance at 1 Hz is likely to be less visible in the responses than one at 10 Hz since the lower frequency resonance has fewer periods to develop.

For the geometric sweep in the experiment, the lower limit of excitation frequency is set to 1 Hz to be able to carry out the sweeps within 30 seconds without having a high frequency ratio. To prevent excessive hinge moments and deflection rates of the gust generator, the upper limit to the excitation frequency is set to 9 Hz. These parameters yield the excitation function in time domain written in equations (1) and (2).

$$\eta(t) = A \cdot \sin(\varphi(t)) \tag{1}$$

$$\varphi(t) = 2\pi f_0 \frac{k^t - 1}{\ln(k)} \tag{2}$$

With

η:	gust generator deflection angle
A:	amplitude of gust generator deflection
φ:	phase angle
f_0:	initial excitation frequency (1 Hz)
k:	exponential factor (1.076)

During the sweeps, quantities such as the wing tip acceleration and the loads acting on the balance are monitored. The sweeps are carried out for each wind speed in Table 3 since the wing's responses also depend on the dynamic pressure.

Time histories of the monitored quantities and the sweep excitations are then subtracted by their corresponding mean values to filter out the static load condition. After the subtraction, a two-pole Bessel lowpass filter [16] is applied to the time histories with a cut-off frequency of 14 Hz. The lowpass filter is intended to filter out the noise in the signal, and the cut-off frequency is selected to prevent having excessive phase and amplitude loss at the upper limit of the excitation range which is 9 Hz. Subsequently, the time histories are transformed into the frequency domain. Transfer functions for each quantity are calculated in the frequency domain through a division of the responses by the excitation as shown in equation (3). To make the transfer functions more intuitive, the input parameter is set to gust speed instead of gust generator deflection angle. The gust speed is calculated using equation (4), whereas a correction factor for the gust speeds according to Lancelot et al. [12] is set to 0.48.

$$TF_{w_g \to y}(f) = \frac{y(f)}{w_g(f)} \tag{3}$$

$$w_g = \sin(\eta) \cdot V_T \cdot k_{wg} \tag{4}$$

With

TF: transfer function
y: response in general
w_g: gust speed
η: gust generator deflection angle
V_T: true flow velocity
k_{wg}: correction factor for gust speed (0.48)

4.2 Rational function approximation

To smooth the trend of each derived transfer function, rational function approximation (RFA) is carried out. The applied RFA employs a curve fitting method using a quotient of polynomials, and it is based on the MATLAB-function polyfit [17] which uses a least-square approach. A parametric example of the rational function is presented in equation (5).

$$p^{RFA}(x) = \frac{a_1 x^n + a_2 x^{n-1} + \cdots + a_n x + a_{n+1}}{b_1 x^d + b_2 x^{d-1} + \cdots + b_d x + b_{d+1}} \tag{5}$$

With

p^{RFA}: resulting quotient of polynomials
x: variable in general
a: numerator coefficients
n: number of polynomial elements in the numerator
b: denominator coefficients
d: number of polynomial elements in the denominator

The frequency range which is to be approximated is limited between 1 and 9 Hz which correlates with the range of the sweep excitation. Outside that range, the signals only show noise and their inclusion would deteriorate the accuracy of the approximation massively. Since only one elastic mode of the wing is expected in the mentioned frequency range, the numbers of necessary poles and zeros in the RFA are expected to be low. However, if the poles and zeros are too few, the accuracy of the approximation is unsatisfactory. On the other hand, if there are more poles and zeros than necessary, sharp amplitude peaks resulting from neighboring poles and zeros might emerge. Moreover, too many poles and zeros might also induce the approximation of the noise in the measured transfer function. For the acceleration and load transfer functions, three poles and three zeros turn out to give satisfactory approximations. Graphs of the approximation results are shown in Section 5.

4.3 Calculation of responses in time domain

Using the transfer function approximations resulting from RFA, the wing's responses to discrete 1-cos gusts and single frequency harmonic gusts are calculated in the frequency domain according to equation (6).

$$y(f) = TF^{RFA}_{w_g \to y}(f) \cdot w_g(f) \tag{6}$$

With

y: response in general
TF^{RFA}: transfer function resulting from RFA
w_g: gust speed

To obtain the responses in the time domain, an inverse Fourier transform is then applied.

5 ACCELERATION AND LOADS RESULTS

The results presented in this section are divided into three categories: static load coefficients, transfer functions and gust responses in time domain. Since the method using transfer function assumes linearity of the observed system, the focus lies in the measurement configuration where the wing is mounted at 0° incidence angle mentioned in Table 3. Moreover, the coordinate system used to analyze the loads is presented in Figure 6, it is equal to the coordinate system shown in Figure 5.

Figure 6: Reference coordinate system

5.1 Static load coefficients

Before the results of the dynamic responses are presented, a comparison of the static load coefficients measured on the wind tunnel model and obtained with the numerical model is conducted. As visualized in the graphs of lift and pitch moment coefficient in Figure 7, the numerical results generally show a very good agreement with the measurement data. In both coefficient graphs, nonlinearities in the experimental data begin to emerge below an angle of attack of -8° and above 10°. Moreover, judging by the lift coefficient markers of different wind speeds lying on top of each other, the effect of the wing's aeroelasticity on the lift slope is negligible.

For the dynamic excitations, with gust vane deflections up to 15° as mentioned in Table 3 and a gust speed correction factor of 0.48 as stated in Section 4.1, the expected amplitude of angle of attack due to gust is approx. 7.5°. Hence, for gust response measurements an incidence angle of 0°, the system is expected to be linear, assuming that no dynamic effects increase the gust angle of attack beyond the linear range.

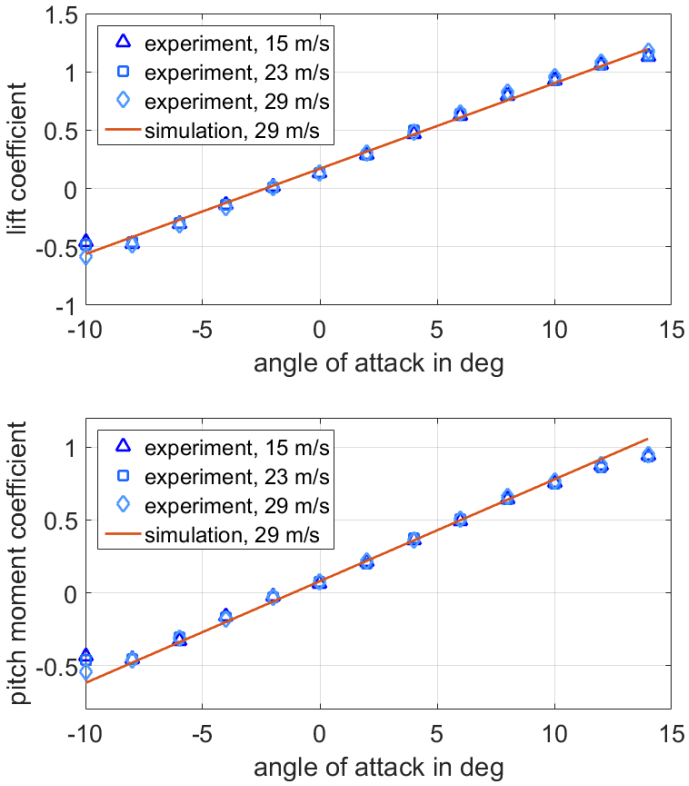

Figure 7: Comparison of static load coefficients

5.2 Transfer functions

Compared to an observation of particular time responses, an observation of transfer functions (TF) in the frequency domain gives a more extensive insight about the dynamic characteristics of the systems. It can also provide a quick overview of resonance frequencies and damping, as shown by the wingtip acceleration transfer functions in Figure 8. The presented transfer functions are calculated using equation (3). Physically, these are equal to responses to ideal white noise gust with an amplitude of 1 m/s at a flow velocity of 29 m/s.
In the amplitude graph, it is apparent that the TF from the experiment has a similar trend as the simulation with MSC.Nastran within the excitation range between 1 and 9 Hz. To smooth the curve of the experimental TF, a rational function approximation (RFA) as explained in Section 4.2 is applied and yields a very good approximation in the excitation range.
Compared to the simulation, there is a slight difference in the frequencies of the peak amplitudes. With RFA, the peak emerges at 5.6 Hz whereas the simulation yields a peak at 5.8 Hz. Besides, the peak amplitudes in both cases are also different: in the simulation, the largest acceleration amplitude is 21.4% larger compared to the experiment. In this case, the wingtip acceleration is a sensitive parameter which depends on e.g. differences in the mass and stiffness distribution between the wind tunnel model and the simulation model.
In the phase diagram, there is a good agreement in phase decrease around the resonance frequency of 5.6 Hz between the experiment and simulation. Here, the smoothing effect of the applied RFA is also visible: in the excitation range, the small local peaks are flattened.
Judging by the transfer function graphs, it can be assumed that the acceleration responses in the experiment are likely to be weaker compared to those in the simulation.

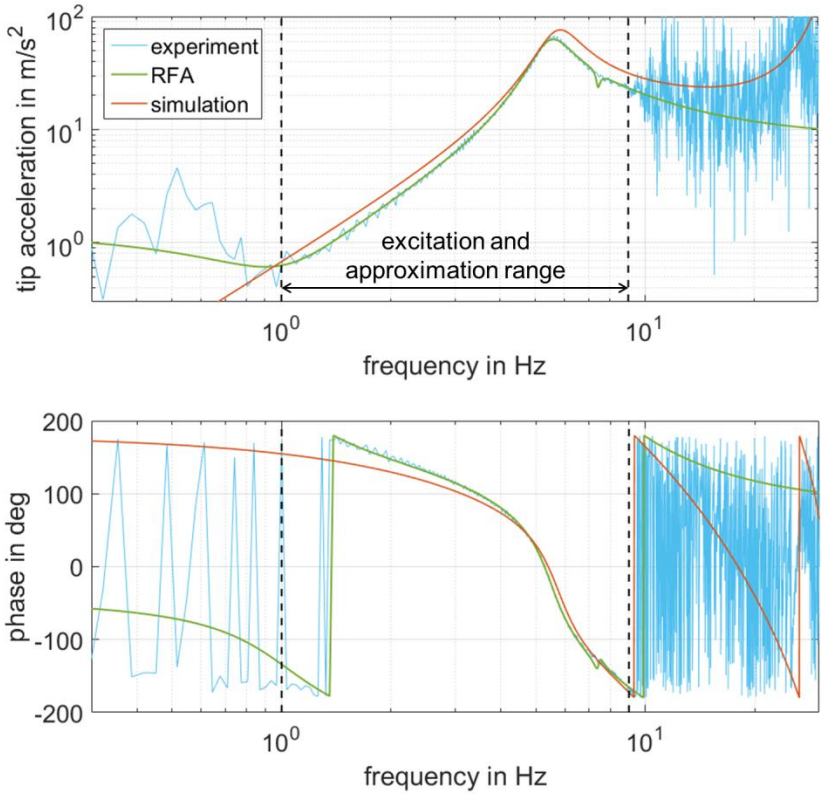

Figure 8: Comparison of acceleration transfer functions at 29 m/s

Another example of transfer function comparison is shown in Figure 9. Here, the observed quantity is the bending moment at a flow velocity of 29 m/s, and the input is ideal white noise gust with an amplitude of 1 m/s.

Similar to the acceleration transfer functions, there is a good agreement between the bending moment curves from the RFA and the simulation. At a low frequency of 1 Hz, the bending moment resulting from the simulation is 3.9% higher compared to the RFA. This is coherent with the very good agreement of the static load coefficients between experiment and simulation. Moreover, the phase curves are nearly identical in the majority of the excitation range, whereas the largest difference is 25° at around 6.5 Hz.

At the first wing bending frequency, it is apparent that the RFA yields a higher peak amplitude compared to the simulation – by 33.6%. Besides, the higher peak despite almost identical amplitude at lower frequencies indicates a lower damping in the experiment. In the simulation, the structural damping is already set relatively low to 1.0%. In the experiment however, the support table bearing the setup shows an eigenfrequency at 5.3 Hz – in the height setting for the experiment. The table's mode couples with the wing's first bending mode, and this explains the observed lower damping in the experiment. Hence, except around the resonance frequency, the bending moment response in the experiment is expected to have very good agreement with the simulation.

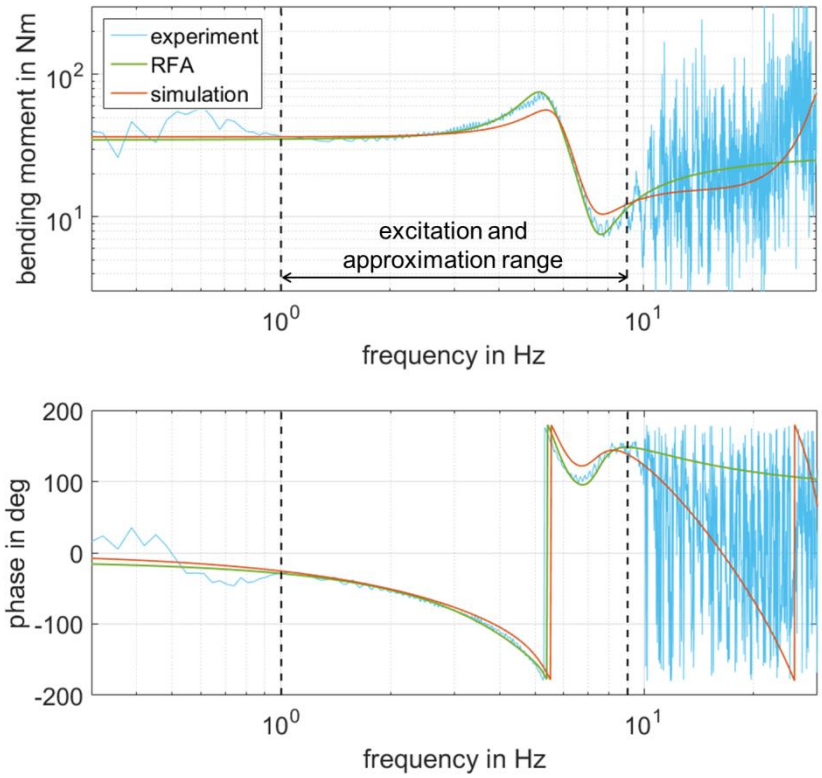

Figure 9: Comparison of bending moment transfer functions at 29 m/s

To observe the effect of flow velocity on the aerodynamic damping, another transfer function comparison of the bending moment is shown in Figure 10. In this case, the flow velocity is 15 m/s, whereas the input is ideal white noise gust with an amplitude of 1 m/s.

Around the resonance frequency of 5.6 Hz, it is apparent that the amplitude peaks – both from the RFA and the simulation – are more pronounced and narrower compared to the ones in Figure 9. This peak characteristic confirms that the aerodynamic damping at 15 m/s is weaker compared to 29 m/s due to the lower dynamic pressure.

At 15 m/s, the relative amplitude difference between the RFA and the simulation results at the resonance frequency is larger. The largest bending moment amplitude resulting from the RFA is 64.3% larger compared to the simulation results (at 29 m/s, the difference is 33.6%). This indicates that the coupling effect with the support table is more pronounced at lower flow velocities.

In the phase diagram in Figure 10, the agreement between the experiment and simulation is not as good as in Figure 9, especially around the resonance frequency. Nevertheless, at lower frequencies around 1 Hz, the phase curves show a very good agreement.

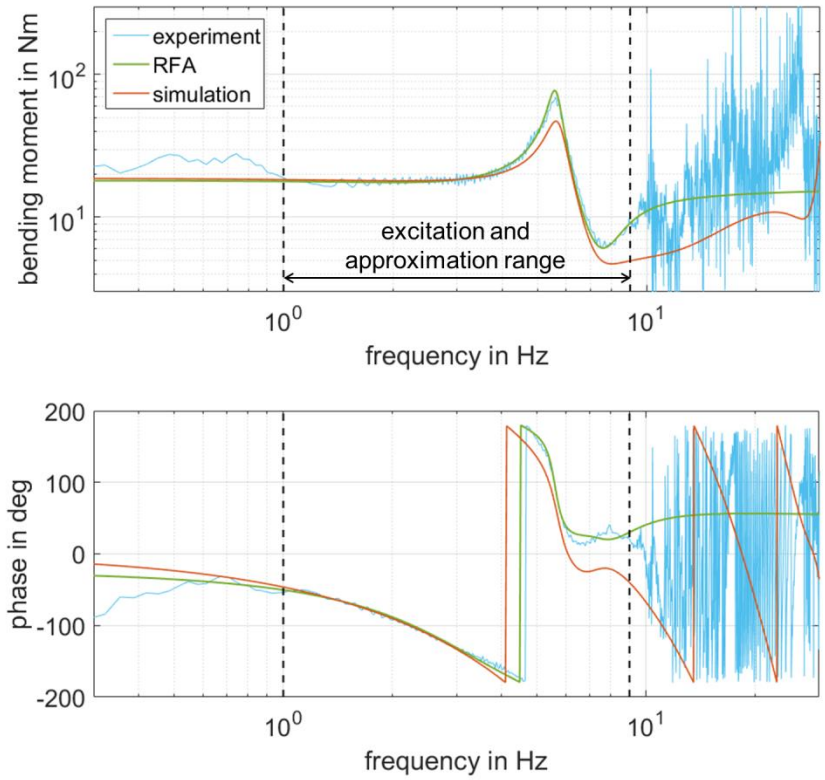

Figure 10: Comparison of bending moment transfer functions at 15 m/s

5.3 Gust responses

For the time domain results, responses to selected discrete 1-cos gusts and single-frequency continuous harmonic gusts are presented. While 1-cos gusts are relevant for design loads in an aircraft design process, the continuous harmonic gusts give an insight into differences in the response amplitudes compared to transient or 1-cos gusts. Moreover, the presented results are incremental values. In other words: if there is no gust, all loads are assumed to be zero.

Discrete 1-cos gust

Since 1-cos gusts are part of the aircraft design load conditions in CS25 [1], the calculation or prediction of the maximum responses to those gusts are of high importance. Judging by the transfer functions presented in Section 5.2, the highest gust loads are expected around the frequency of the first wing bending. Hence, the comparison of the gust responses is conducted using the 5.6 Hz gust mentioned in Table 3. Since the bending moment has a large influence on the wing structural mass, the focus is set to observing the largest bending moment responses. The latter occur at high flow velocities, and in this experiment, it is 29 m/s. Moreover, the selected measurements are those with the maximum gust vane deflection of 10° to maximize the signal to noise ratio.

Figure 11 shows a comparison of the bending moment response to a 5.6 Hz discrete gust between three methods: experiment, semi-experimental method, simulation. The reduced frequency of the gust excitation is 0.146. As a remark: the two-pole Bessel lowpass filter with a cut-off frequency of 14 Hz has also been applied to the presented experimental data to mitigate noise. Moreover, the term semi-experimental method implies the use of transfer functions approximated using RFA to calculate the time domain response. Its methodology is described in Section 4 and the approximations of the experimental transfer functions are shown in Section 5.2.

In the bending moment response, it is apparent that all three curves have very good agreement in the maximum value and the decay. The highest value is obtained using the semi-experimental method, whereas the maximum in the experiment is 4.4% smaller and in the simulation 5.1% smaller. The slightly lower maximum value in the simulation emerges through the lower values in the transfer function shown in Figure 9 around the frequency 5.6 Hz.

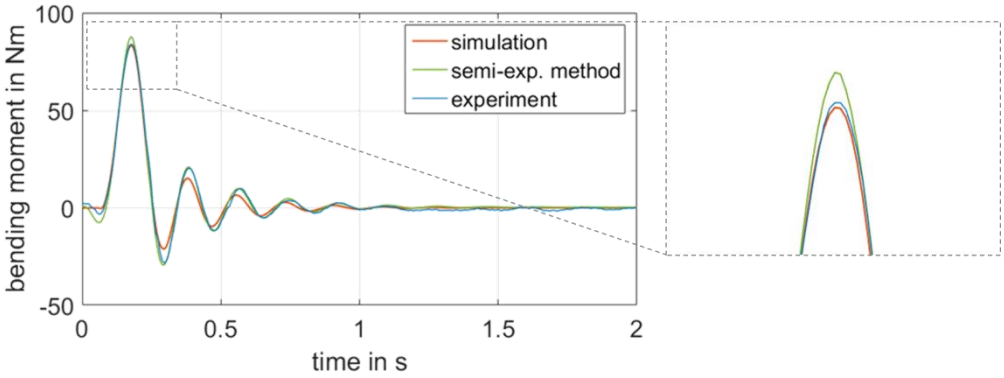

Figure 11: Bending moment response to a 5.6 Hz discrete gust at 29 m/s

Another comparison for a crosscheck with the transfer functions is the wingtip acceleration as presented in Figure 12. Compared to the semi-experimental method, the peak value in the simulation is 20.4% larger, while the maximum in the experiment is 10.8% smaller. As mentioned in Section 5.2, the wingtip acceleration is a parameter which is sensitive to deviations in the mass and stiffness distribution of the wing. Hence, slight differences between the simulation model and the actual wind tunnel model can have a large impact on the wingtip acceleration, while e.g. the bending moment is hardly influenced.

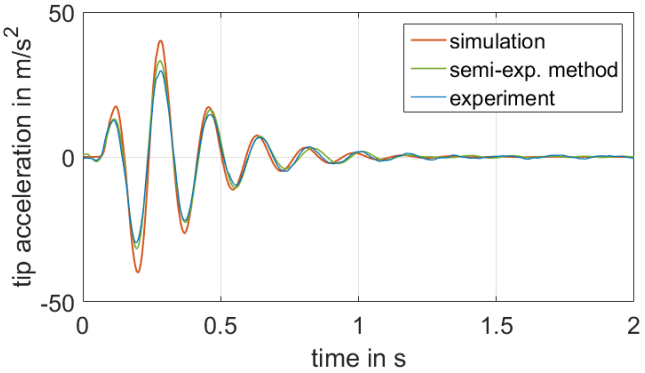

Figure 12: Acceleration response to a 5.6 Hz discrete gust at 29 m/s

To observe the dependency of the bending moment response on the gust frequency, another comparison with a 1 Hz discrete gust is presented in Figure 13, and its reduced frequency is 0.026. This gust frequency is also interesting since it is at the lower limit of the excitation range with which the transfer functions in the semi-experimental method are approximated, as mentioned in Section 4. The maximum bending moment in obtained in the simulation is larger by 5.1% compared to the semi-experimental method. This is coherent to the bending moment transfer functions in Figure 9 where the simulation yields a slightly higher value at 1 Hz than RFA. On the other hand, the experiment yields 4.1% less maximum bending moment compared to the semi-experimental method.

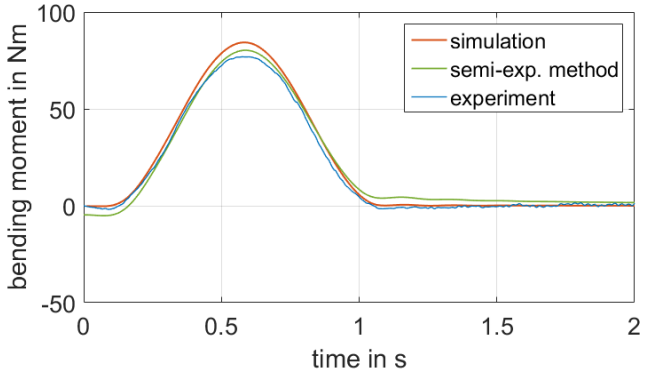

Figure 13: Bending moment response to a 1 Hz discrete gust at 29 m/s

Continuous harmonic gust

Beside 1-cos gusts which are relevant for aircraft structure design, continuous harmonic gusts are also relevant for certain phenomena, e.g. whether the discrete gusts have transient effects which lead to different maximum values compared to continuous gusts.

Figure 14 shows a comparison of a continuous gust with an excitation frequency of 5.6 Hz, at 29 m/s flow velocity and 10° gust vane deflection amplitude. The peak value obtained in the simulation is 9.3% smaller compared to the semi-experimental method which is coherent to the transfer functions shown in Figure 9. This difference is larger than during a 1-cos gust (5.1%) and this is caused by following:

- The spectrum of a continuous gust is a single peak at the excitation frequency, while a 1-cos gust has a broader spectrum.
- Hence, for a continuous gust, the value of the transfer function at the excitation frequency – in this case 5.6 Hz – has a larger influence on the response.
- This means, any deviation of the transfer function value at the excitation frequency is more clearly visible in the response to a continuous gust rather than a 1-cos gust.

On the other hand, the average peak value measured in the experiment is 13.0% smaller compared to the semi-experimental method. This difference is also larger than that emerging with 1-cos gust (4.4%). This is explained by following points:

- In the transfer function in Figure 9, the bending moment reaches the maximum value at 5.2 Hz
- During the sweep which is used for the transfer function generation, the excitation frequency increases with a ratio of 1.076 per second (equations (1) and (2))
- The excitation frequency 5.6 Hz is reached less than a second after the peak resonance at 5.2 Hz
- The resonance has not decayed completely, and the residue of the oscillation potentially increases the response at 5.6 Hz
- Therefore, the derived transfer function shows a higher value at 5.6 Hz compared to the system's actual characteristics.

To quantify the influence of this phenomenon, a sweep excitation with a lower frequency ratio/progress is advisable. With that, the peak resonance at 5.2 Hz has more time to decay before the excitation frequency has increased much.

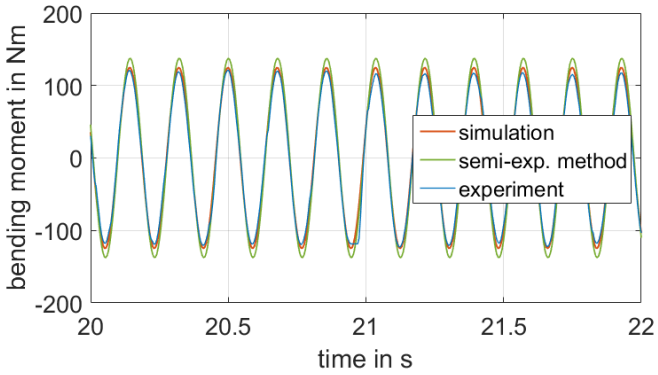

Figure 14: Bending moment response to a 5.6 Hz continuous gust at 29 m/s

Another comparison to investigate is the time responses to a continuous gust with 1 Hz excitation frequency as visualized in Figure 15. Here, coherent to the transfer function in Figure 9 and the response to a 1-cos gust in Figure 13, the simulation also yields a slightly larger bending moment compared to the semi-experimental method. In the peak values, the simulation yields 3.9% higher bending moment. On the other hand, the average peak value obtained in the experimental measurement is 5.3% smaller than the semi-experimental method. This is also coherent with all other time responses that the measured data show slightly lower values compared to the semi-experimental method.

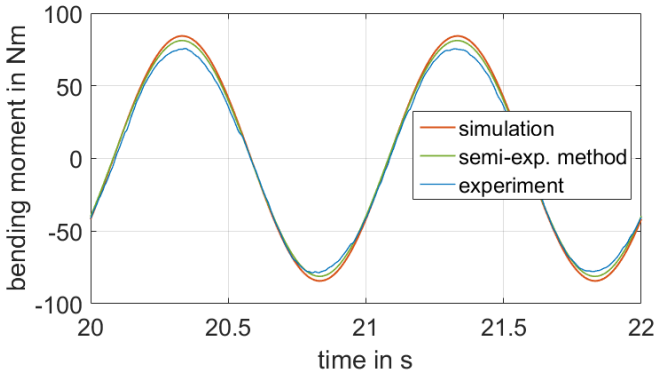

Figure 15: Bending moment response to a 1 Hz continuous gust at 29 m/s

6 CONCLUSION AND OUTLOOK

The proposed semi-experimental method enables a prediction of the wing's response to any gust using transfer functions derived from measurements. In the measurements, sweep excitations are introduced using the gust generator.

In the ideal case, the advantage of this semi-experimental prediction method mainly lies in the reduction of wind tunnel time. Instead of testing each gust profile at each frequency, a measurement of several sweep excitations would suffice.

To obtain more accurate results of the wing's response to a gust, the sweep excitation should cover the frequency range of the gust. Or vice versa: with a given sweep excitation, the gust's frequency content should lie within the frequency range of the sweep. Furthermore, the proposed method is more reliable in predicting responses to gusts with a broad spectrum such as 1-cos gusts rather than single-frequency continuous harmonic gusts.

By observing the responses to discrete and continuous gusts, it is apparent that a continuous excitation around the resonance frequency results in significantly stronger responses compared to a discrete gust excitation with the same frequency. As a result, for wind tunnel models sized using discrete gusts, it is advisable to reduce the excitation amplitude if they are tested with continuous gusts.
For the future, investigations using data from measurements with an incidence angle of 4° and 10° are planned. With these data, the influence of aerodynamic nonlinearities on the accuracy of the method can be quantified. Furthermore, a model update for the wing with the tip mass can also be considered to obtain a better agreement between the simulation and experimental results.

7 REFERENCES

[1] European Aviation Safety Agency, "CS25 - Certification Specifications and Acceptable Means of Compliance for Large Aeroplanes - Amendment 16." 2015.

[2] European Aviation Safety Agency, "JAR25 - Joint Aviation Requirements – Large Aeroplanes, Change 14, Joint Aviation Authorities." 1994.

[3] Krüger, W., Klimmek, T., Liepelt, R., Schmidt, H., Waitz, S., Cumnuantip, S. Design and aeroelastic assessment of a forward-swept wing aircraft. in *CEAS Aeronautical Journal Vol. 5*, 2014.

[4] Seitz, A., Kruse, M., Wunderlich, T., Bold, J., Heinrich, L. The DLR Project LamAiR: Design of a NLF Forward Swept Wing for Short and Medium Range Transport Application. in 29th *AIAA Applied Aerodynamics Conference*, 2011.

[5] Meddaikar, Y. M., Dillinger, J. K. S., Ritter, M., Govers, Y. Optimization & Testing of Aeroelastically-Tailored Forward Swept Wings. in *International Forum on Aeroelasticity and Structural Dynamics, IFASD 2017*, 2017.

[6] Dillinger, J. K. S., Klimmek, T., Abdalla, M. M., Gürdal, Z. Stiffness Optimization of Composite Wings with Aeroelastic Constraints. *Journal of Aircraft Volume 50, Number 4*, 2013, pages 1159-1168.

[7] Dillinger, J. K. S., Abdalla, M. M., Klimmek, T., Gurdal, Z. Static Aeroelastic Stiffness Optimization and Investigation of Forward Swept Composite Wings. Orlando, Florida, USA, 2013.

[8] Meddaikar, Y. M., Irisarri, F. X., Abdalla, M. M. Laminate optimization of blended composite structures using a modified Shepard's method and stacking sequence tables. *Structural and Multidisciplinary Optimization Volume 55, Number 2*, 2017, pages 535-546.

[9] Dillinger, J.K.S. Static Aeroelastic Optimization of Composite Wings with Variable Stiffness Laminate. Delft University of Technology, 2014.

[10] Meddaikar, Y. M., Dillinger, J. K. S., Sodja, J., Mai, H., De Breuker, R. Optimization, Manufacturing and Testing of a Composite Wing with Maximized Tip Deflection. San Diego, California, USA, 2016.

[11] Ritter, M., Meddaikar, Y.N., Dillinger, J. Static and Dynamic Aeroelastic Validation of a Flexible Forward Swept Composite Wing. *58th AIAA/ASCE/AHS/ASC Structures, Structural Dynamics, and Materials Conference. AIAA SciTech 2017*, Grapevine, Texas, USA, 2017.

[12] Lancelot, P. M. G. J., Sodja, J. & De Breuker, R. Investigation of the Unsteady Flow Over a Wing Under Gust Excitation. in *International Forum on Aeroelasticity and Structural Dynamics, IFASD 2017,* 2017.

[13] Lancelot, P. M. G. J., Sodja, J., Werter, N. P. M. & De Breuker, R. Design and testing of a low subsonic wind tunnel gust generator. *Advances in Aircraft and Spacecraft Science Volume 4, Number 2*, March 2017, pages 125-144.
[14] Govers, Y. und Meddaikar, Y.M., Sinha, K. Model validation of an aeroelastically-tailored forward swept wing using fibre-optical strain measurements. in: *Proceedings of ISMA2018 International Conference on Noise and Vibration* Engineering, ISMA 2018, 2018.
[15] PCB, "Model 356A45 Triaxial ICP ® Accelerometer Installation and Operating Manual." [Online]. Available: https://www.pcb.com/products.aspx?m=356A45. [Accessed: 30-Apr-2019].
[16] ScienceDirect, "Bessel Filter." [Online]. Available: https://www.sciencedirect.com/topics/engineering/bessel-filter. [Accessed: 09-May-2019].
[17] Mathworks, "Documentation – MATLAB – Mathematics – Elementary Math – Polynomials – polyfit". [Online]. Available: https://de.mathworks.com/help/matlab/ref/polyfit.html [Accessed: 09-May-2019].

COPYRIGHT STATEMENT